Article

Effect of Composition on the Optical and Photocatalytic Properties of Visible Light Responsive Materials $Bi_{26-x}Mg_xO_{40}$

Dmitry S. Shtarev,* Ruslan Kevorkyants, Maxim S. Molokeev, and Anna V. Shtareva

Read Online

ACCESS | Metrics & More | Article Recommendations | SI Supporting Information

ABSTRACT: We report the synthesis and the crystal and electronic structure as well as the optical and photocatalytic properties of novel photoactive materials of the general formula $Bi_{26-x}Mg_xO_{40}$. Two compounds with compositions of $Bi_{24.28(3)}Mg_{1.72(3)}O_{40}$ and $Bi_{24.05(3)}Mg_{1.95(3)}O_{40}$ are synthesized using the pyrolytic method. According to X-ray diffraction analysis, the materials are monocrystalline species. Their electronic bandgaps determined from Tauc plots are 2.41 eV $[Bi_{24.28(3)}Mg_{1.72(3)}O_{40}]$ and 2.69 eV $[Bi_{24.05(3)}Mg_{1.95(3)}O_{40}]$. Keeping in mind that optical bandgaps are typically larger than their electronic counterparts, we find that the bismuthate bandgaps match well that of $Bi_{24}Mg_2O_{40}$ (2.26 eV) predicted by density functional theory. Apparently, the synthesized bismuthates are indirect bandgap semiconductors just like $Bi_{24}Mg_2O_{40}$. Both materials demonstrate nearly identical luminescence spectra. Their luminescence emission at 620 nm is most efficiently excited by 365 nm light. The materials' photocatalytic properties are evaluated in a visible light-induced photocatalytic phenol degradation reaction. Rather low activity of both compounds is detected. However, $Bi_{24.05(3)}Mg_{1.95(3)}O_{40}$ is ~2 times more photocatalytically active than $Bi_{24.28(3)}Mg_{1.72(3)}O_{40}$, which is associated with a higher Bi^{5+} content in the former.
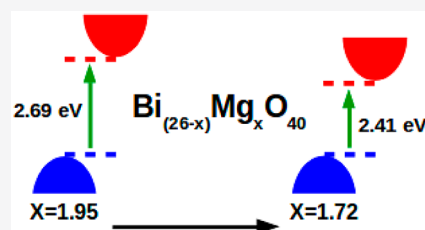
1. INTRODUCTION

Metal oxides make up a large family of chemical compounds that are used in various technological applications. One of them, the bismuth oxide Bi_2O_3, is represented by the four well-known polymorphs (α, β, γ, and δ) and the two more recently discovered ones (ω and ε). The first four polymorphs exhibit electric conductance, which can be of the electronic or ionic type. For this reason, they can be used in solid oxide fuel cells or utilized as oxygen sensors.

The bismuth oxide polymorph of our particular interest to us is the γ-Bi_2O_3 phase because it may incorporate various metal cations forming a group of compounds called sillenites. In its simple form, the general formula of sillenites can be written using the format suggested by Valant and Suvorov, $Bi_{12}(Bi^{3+}_{4/5-nx}M^{n+}_{5x})O_{19.2+nx}$,[1] where M represents a metal cation at the tetrahedral site, n stands for the charge of the dopant cation M, and x denotes the upper metal cation's substitution limit. The ideal stoichiometric sillenite structure $Bi_{12}M^{4+}O_{20}$ contains the metal cation M^{4+} at a tetrahedral site. Formally, such a sillenite compound can be represented as $[6Bi_2O_3 \cdot MO_2]$. In addition, sillenite structures may possess M cations with oxidation states varying from 2+ to 5+ giving rise to some 60 species.

The members of alkaline-earth sillenite subfamily are known to act as visible light photocatalysts. One factor that enables such behavior is a recently established trend in the empirical dependence of valence and conduction band energy positions on the materials' bandgaps.[2] In contrast to calcium,[3−11] strontium,[12−20] and barium[21−25] bismuthates, which have been widely studied, little is known about magnesium bismuthates.[26]

The primary goal of our work is to elaborate a preparation route of monophase $Bi_{26-x}Mg_xO_{40}$ samples that is followed by the study of their optical and photocatalytic properties. According to the earlier reports, the photocatalytic activity of bismuthates depends on the relative concentration of their constituent metal cations.[3] Here, we address this issue with respect to the monophase $Bi_{26-x}Mg_xO_{40}$ samples.

2. EXPERIMENTAL SECTION

In this section, we describe the experimental methods used to prepare, characterize, and evaluate the photocatalytic activity of magnesium bismuthate samples $Bi_{26-x}Mg_xO_{40}$.

2.1. Synthesis. The samples $Bi_{26-x}Mg_xO_{40}$ were prepared by the pyrolytic method, which has been proven to be successful in the synthesis of calcium bismuthates.[3] The chemical purity of the utilized reactants $Bi(NO_3)_3 \cdot 5H_2O$, $Mg(NO_3)_2 \cdot 6H_2O$, and sorbitol $C_6H_{14}O_6$ exceeded 99.0%. First, the reactants were ground, resulting in the formation of a viscous transparent solution that was due to water in the crystalline hydrates. The solution was kept at room temperature for 24 h. At this stage, the nitration of sorbitol by the nitrates took place, thereby turning the viscous transparent solution into a yellow foam-like solid. Then, the formed solid was homogenized and pyrolyzed at 350 °C for 4 h, leading to decomposition of the organic matrix and elimination of the remaining pyrolytic carbon. At this

Table 1. Details of the Preparation of the $Bi_{26-x}Mg_xO_{40}$ Samples

sample	$[Mg][Mg] + [Bi]$ (%)	precursor mass (g)			T (°C)	t (h)
		$Mg(NO_3)_2 \cdot 6H_2O$	$Bi(NO_3)_3 \cdot 5H_2O$	sorbitol		
BiMgO-1.00	1.00	0.02563	4.8015	0.90781	800	96
BiMgO-7.69	7.69	0.17941	4.0740	0.80762	800	96

stage, a mixture of magnesium and bismuth oxides was obtained. Eventually, the target oxide phases were produced by heating the reaction mixture at 800 °C for 96 h. Following this synthetic route, two $Bi_{26-x}Mg_xO_{40}$ samples featuring different Mg:Bi ratios were prepared. They are abbreviated as BiMgO-1.00 and BiMgO-7.69. The $[Mg]/([Mg] + [Bi])$ ratios in the former and latter compounds were 1.00% and 7.69%, respectively. The applied synthesis conditions are summarized in Table 1.

During the last stage of preparation, the chosen pyrolytic route is similar to the triphase method. Annealing of two oxides results in a formation of a new crystalline compound, magnesium bismuthate. The annealing stage of the preparation of magnesium bismuthates is the most tedious because of the large difference in the oxides' melting points (817 and 2825 °C for Bi_2O_3 and MgO, respectively). For this reason, the formation of the magnesium bismuthate crystal lattice takes a rather long time and requires thorough control.

According to Table 1, the annealing temperature was set to 800 °C. This value is close to the melting point of Bi_2O_3. Therefore, during the lengthy annealing process, a partial evaporation of the oxide was expected. This enabled us to control the Mg:Bi ratio in the samples. That is, to prepare the BiMgO-7.69 phase, the annealing was conducted in a covered crucible. In contrast, the annealing of BiMgO-1.00 was performed without a crucible cover. Samples prepared using the procedure described above were expected to contain a single phase and different Bi:Mg ratios in the cationic sublattice.

2.2. Characterization. The samples' phase composition was examined by X-ray diffraction (XRD). Powder diffraction data for Rietveld analysis were collected at room temperature using a Bruker D8 ADVANCE powder diffractometer with Cu Kα radiation and a linear VANTEC detector. XRD data collection was carried out in the 2θ range of 10−110°. The 2θ data collecting interval and time were 0.016° and 1 s, respectively. The Rietveld refinement was performed using TOPAS 4.2.[27]

The sample's morphology was determined by scanning electron microscopy (SEM; TESCAN, acceleration voltage of 20 kV). The element composition and its distribution in the synthesized magnesium bismuthate samples were established by energy dispersive X-ray spectroscopy (EDX; X-MaxN, Oxford Instruments).

The composition of elements on the surface and the valence band position were determined by X-ray photoelectron spectroscopy (XPS) using a Thermo Fisher Scientific Escalab 250Xi spectrometer (Al Kα radiation, 1486.6 eV; spectral resolution, 0.5 eV); the reference carbon line Cls (C−C bond) was taken at the binding energy of 284.8 eV.[28]

Diffuse reflectance spectra, as $R(\lambda)$, were recorded in the spectral range of 375−775 nm under ambient conditions using a Cary 5000 UV/vis/NIR spectrophotometer equipped with a DRA 2500 external diffuse reflectance accessory; optical-grade $BaSO_4$ powder was used as a reference standard.

The chemical composition of the synthesized samples and, in particular, the Bi:Mg ratio were determined via inductively coupled plasma mass spectrometry (ICP-MS, Elan 9000, PerkinElmer). The spectrometer was graduated utilizing polyelemental solutions provided by PerkinElmer. The isotope ^{115}In was used as an intrinsic standard, which was added to all of the samples at a concentration of 40 μg/L. The following operational settings and conditions were applied: high-frequency generator power, 1350 W; nebulizer gas flow rate, 0.93−0.95 L/min; sensitivity with respect to ^{115}In (standard solution concentration of 10 μg/L), 6×10^5 cps; scanning regime, peak hopping; oxide level, <3%; M^{2+} level, <3%.

2.3. Evaluation of Photocatalytic Activity. The photocatalytic activity of the prepared magnesium bismuthate samples was tested in a simulated solar light-assisted degradation reaction of phenol in its aqueous solution. The phenol concentration (≥99.5% purity, ACROS Chemicals) was equal to 100 ppm. For a typical photocatalytic test, 300 mg of the bismuthate sample and 300 mL of the aqueous phenol solution were used.

Before irradiation, the reaction mixture was kept in the dark for 30 min, which was necessary to reach the adsorption−desorption equilibrium between the bismuthate sample and phenol. The 150 W xenon lamp (Osram) with a 310 nm cutoff filter (light irradiance, 7 mW cm^{-2}) served as the source of simulated solar (ultraviolet and visible) light. Concentrations of phenol in the reaction mixture were analyzed by high-performance liquid chromatography (HPLC) at certain time intervals. Prior to HPLC analysis, probes were filtered through the 0.2 μm Minisart filter to remove solid particles. The analysis was performed using a model 1260 Infinity liquid chromatograph equipped with an ultraviolet−visible detector and C18 column (Agilent Technologies). The mobile phase was a 50:50 (v/v) methanol/water mixture; the detection wavelength was 210 nm at a bandwidth of 4 nm.

The photocatalytic reaction was used as a measure of the photocatalytic activity of the bismuthates. Its initial rate was estimated from the following kinetic approximation:

$$c(t) = c_0 \exp(-kt) \tag{1}$$

$$dC/dt_{(t\to0)} = -kC_0 \tag{2}$$

where k is an apparent quasi-first-order rate constant.

Hereafter, by activity, we mean the value of k determined by the method described above.

3. COMPUTATIONAL DETAILS

The electronic structure of the magnesium bismuthates was modeled using the periodic density functional theory (DFT) approach. For this purpose, the GGA Perdew−Burke−Ernzerhof (PBE) density functional[29,30] as implemented in the ABINIT 6.8.3 program[31] was chosen. The basis set in the form of the Troullier−Martins norm-conserving pseudopotentials[32] with a kinetic energy cutoff of 30 Hartree was employed. The $I2_3$ space symmetry of the material's crystal lattice determined by XRD was enforced. The Brillouin zone (BZ) was sampled over the automatically generated Γ-point-centered $4 \times 4 \times 4$ Monkhorst−Pack grid of k-points.[33] The electronic band structure was computed at 81 k-points along the Γ−M−R−X−Γ high-symmetry path of a cubic BZ. The default total energy convergence criterion of 1.0×10^{-8} Hartree was applied. Band structures and densities of states were plotted using the Gnuplot 5.2 software package.[34]

4. RESULTS AND DISCUSSION

4.1. Crystal Structure and Composition of the Samples. During the synthesis, the BiMgO-1.00 and BiMgO-7.69 samples were controlled by SEM and XRD. Panels a and c of Figure S1 depict SEM images of the typical samples' particles formed after annealing for 24 h at 800 °C. Particles of both bismuthate samples contain inclusions of a second phase seen as the darker image areas. This second phase is found to be MgO. The corresponding XRD images are presented in panels b and d of Figure S1. According to the
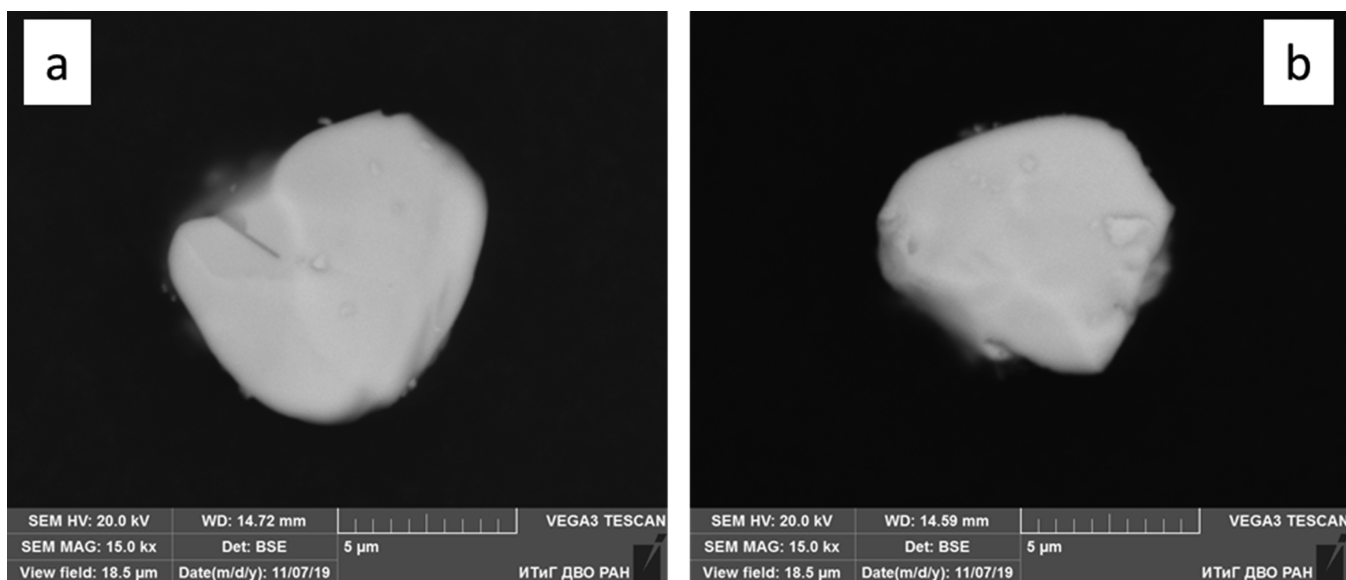
Figure 1. SEM images of typical (a) BiMgO-7.69 and (b) BiMgO-1.00 particles obtained after annealing of the reaction mixture for 96 h at 800 °C.
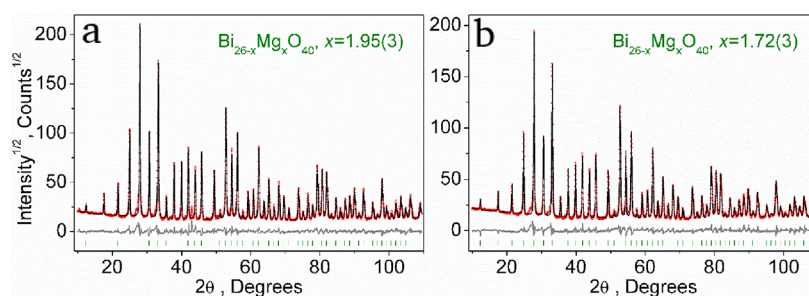

Figure 2. Difference Rietveld plot of $Bi_{26-x}Mg_xO_{40}$: (a) MgBiO-7.69 [x = 1.95 (3)] and (b) MgBiO-1.00 [x = 1.72 (3)]. Red dots show the experimental XRD powder pattern. The black solid line shows the patterns calculated from the structure. The gray solid line shows the difference between experimental and calculated patterns. The green vertical lines show Bragg peak positions.

figures, the Bi_2O_3 and MgO phases coexist with the newly formed $Bi_{26-x}Mg_xO_{40}$ phase in the samples. Thus, the bismuthate's phase formation was not yet completed. The SEM images of the bismuthate samples annealed for an additional 24 h (panels c and c of Figure S2) still show the presence of the pure metal oxides' phases. This is consistent with the corresponding XRD images in panels b and d of Figure S2 demonstrating that the new $Bi_{26-x}Mg_xO_{40}$ phase continues to form. After annealing of the bismuthate samples for 48 h at 800 °C, the content of pure metal oxides is decreased, whereas that of $Bi_{26-x}Mg_xO_{40}$ is increased compared to their contents in the samples annealed at the same temperature for 24 h. This trend also holds for annealing of the samples for 72 h at 800 °C: the number of pure metal oxide inclusions and their size decrease (panels a and c of Figure S3), whereas the content of the $Bi_{26-x}Mg_xO_{40}$ phase increases (panels b and d of Figure S3).

The formation of monophase $Bi_{26-x}Mg_xO_{40}$ samples succeeded only after annealing at the set temperature for 96 h (Figure 1). The figure shows that annealing of both BiMgO-1.00 and BiMgO-7.69 samples results in a similar particle size. The particles' surfaces lack pores and fractures.

The structure and unit cell composition of the synthesized magnesium bismuthates were studied by XRD. Figure 2 presents the obtained X-ray diffraction pattern and results of Rietveld analysis of the two $Bi_{26-x}Mg_xO_{40}$ samples. Therein, all

peaks were indexed by a cubic unit cell (symmetry space group $I2_3$) with parameters close to those of $Bi_{24}Si_2O_{40}$.[35] Therefore, this crystal structure was taken as a model for the Rietveld refinement. The refinement was stable and gave low R factors (Table 2). In the bismuthate structures, the Si site was occupied by either a Bi cation or a Mg cation. The cation ratio was determined. Chemical formulas of the compounds established using the refinement can be written as $Bi_{24.05(3)}Mg_{1.95(3)}O_{40}$ (BiMgO-7.69 sample) and $Bi_{24.28(3)}Mg_{1.72(3)}O_{40}$ (BiMgO-1.00 sample) (Figure 2). The crystallographic data have been deposited in the Cambridge

Table 2. Unit Cell and Rietveld Refinement Parameters of the Bismuthate Samples

	MgBiO-7.69	MgBiO-1.00
compound	$Bi_{24.05(3)}Mg_{1.95(3)}O_{40}$	$Bi_{24.28(3)}Mg_{1.72(3)}O_{40}$
space group	$I23$	$I23$
a (Å)	10.1104 (1)	10.1244 (2)
V (Å^3)	1033.49 (4)	1037.80 (5)
2θ interval (deg)	10−110	10−110
R_{wp} (%)	10.28	11.13
R_P (%)	7.37	7.91
R_{exp} (%)	3.67	3.75
χ^2	2.80	2.97
R_B (%)	2.72	3.82

Crystallographic Data Centre [CSD 1979141 for $Bi_{24.05(3)}Mg_{1.95(3)}O_{40}$ and CSD 1979140 for $Bi_{24.28(3)}Mg_{1.72(3)}O_{40}$]. Graphically, the magnesium bismuthate's crystal structure with a generic chemical formula of $Bi_{26-x}Mg_xO_{40}$ is shown in Figure 3. Presumably, this structure

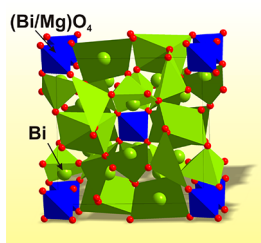**Figure 3.** $Bi_{26-x}Mg_xO_{40}$ crystal structure. The green octahedra and blue tetrahedra denote BiO_8 and $(Bi/Mg)O_4$ structural units, respectively. Green and red spheres are Bi and O, respectively.

should have oxygen vacancies. Because their positions are hard to refine from the powder patterns, we left the oxygen content in the chemical formulas unchanged. Table 2 shows that the bismuthate's unit cell volume decreases as the Mg concentration increases. Given the same space symmetry of both compounds and the fact that the ionic radius of Mg is smaller than that of Bi, this trend is quite expected. Atomic coordinates and main bond lengths of the bismuthate compounds are listed in Tables 3 and 4, respectively.

The studied bismuthate $Bi_{26-x}Mg_xO_{40}$ can be seen as the bismuth oxide $Bi_{26}O_{40}$ in which a fraction of Bi cations in its cationic sublattice is substituted by Mg ones. The oxide contains 25 Bi^{3+} cations and one Bi^{5+} cation and thus can be represented by the formula $Bi^{3+}_{25}Bi^{5+}O_{40}$. Table 3 shows that Mg can substitute for Bi only at position (0; 0; 0). Indeed, according to the XRD analysis, in MgBiO-7.69 the Mg^{2+} cation occupies this position with a probability of 97.7%, whereas in MgBiO-1.00, it occupies this position with a probability of 85.8%.

Now, let us determine the contents of Bi^{3+} and Bi^{5+} cations in the bismuthates. This can be done by solving a system of linear equations, which involves an electronic balance and the content of Bi in the compounds. In the case of $Bi_{24.05(3)}Mg_{1.95(3)}O_{40}$, we obtain the following electronic balance equation: $1.95 \times 2 + x \times 3 + y \times 5 = 80$, where the

Table 4. $Bi_{26-x}Mg_xO_{40}$ Bond Lengths (Å)

	MgBiO-7.69 [$Bi_{24.05(3)}Mg_{1.95(3)}O_{40}$]		
Bi1−O1[a]	2.199 (15)	Bi1−O2[e]	2.29 (3)
Bi1−O2[b]	2.049 (15)	Bi1−O3[b]	2.60 (2)
Bi1−O2[c]	3.14 (3)	Bi2−O3[e]	1.77 (2)
Bi1−O2[g]	3.00 (3)	Mg−O3[f]	1.77 (2)
Bi1−O2[d]	2.62 (3)		
	MgBiO-1.00 [$Bi_{24.28(3)}Mg_{1.72(3)}O_{40}$]		
Bi1−O1[a]	2.176 (16)	Bi1−O2[e]	2.13 (3)
Bi1−O2[b]	2.189 (16)	Bi1−O3[b]	2.59 (2)
Bi1−O2[c]	3.13 (3)	Bi2−O3[f]	1.75 (2)
Bi1−O2[d]	2.63 (3)	Mg−O3[f]	1.75 (2)

[a]Symmetry codes: $z - 1/2$, $x - 1/2$, $y - 1/2$. [b]Symmetry codes: $-x + 1$, $-y + 1$, $z - 1$. [c]Symmetry codes: $-z + 1$, $-x + 1$, $y - 1$. [d]Symmetry codes: $y - 1/2$, $-z + 3/2$, $-x + 1/2$. [e]Symmetry codes: $y - 1/2$, $z - 1/2$, $x - 1/2$. [f]Symmetry codes: $x - 1$, $y - 1$, $z - 1$. [g]Symmetry codes: $z - 1$, $-x + 1$, $-y + 1$.

numbers 2, 3, and 5 are the oxidation states of Mg^{2+}, Bi^{3+}, and Bi^{5+} cations, respectively. The corresponding multipliers are coefficients in the chemical formula $Bi^{3+}_xBi^{5+}_yMg_{1.95}O_{40}$. The second equation $x + y = 24.05$ limits the total amount of Bi in both oxidation states to its determined value of 24.05. Having solved the system of equations, we obtain $Bi^{3+}_{22.075}Bi^{5+}_{1.975}Mg_{1.95}O_{40}$, which matches well the chemical formula of $Bi_{24}Mg_2O_{40}$. Similarly, the second bismuthate can be represented by the chemical formula $Bi^{3+}_{22.42}Bi^{5+}_{1.86}Mg_{1.72}O_{40}$. Thus, by changing the concentration of Mg in a bismuthate, one can control its Bi^{5+} content.

The chemical compositions of the bismuthates were investigated by EDX. Figures S4 and S5 show EDX maps of the typical bismuthate particles. Table S1 lists the data for the distribution of Mg and Bi in a large number of the bismuthate particles obtained by statistical analysis. Therein, concentrations of the metal cations differ from those established by XRD that is due to the insufficient sensitivity of EDX. However, both methods predict a higher concentration of Mg and a lower concentration of Bi in the MgBiO-7.69 sample than in the MgBiO-1.00 sample.

In addition to the used XRD and EDX analysis techniques, we have also conducted an ICP-MS study of the bismuthate samples. The results of the latter are listed in Table S2. According to the table, the concentrations of Mg^{2+} in the cationic sublattices of MgBiO-1.00 and MgBiO-7.69 were

Table 3. $Bi_{26-x}Mg_xO_{40}$ Fractional Atomic Coordinates and Isotropic Displacement Parameters (Å²)

| atom	x	y	z	B_{iso}	occupancy
		MgBiO-7.69 [$Bi_{24.05(3)}Mg_{1.95(3)}O_{40}$]			
Bi1	0.17562 (12)	0.31771 (9)	0.01597 (9)	0.73 (4)	1
Bi2	0	0	0	3.1 (13)	0.023 (17)
Mg	0	0	0	3.1 (13)	0.977 (17)
O1	0.6937 (15)	0.6937 (15)	0.6937 (15)	3.2 (5)	1
O2	0.6378 (14)	0.7570 (18)	0.990 (3)	3.2 (5)	1
O3	0.899 (2)	0.899 (2)	0.899 (2)	3.2 (5)	1
		MgBiO-1.00 [$Bi_{24.28(3)}Mg_{1.72(3)}O_{40}$]			
Bi1	0.17479 (12)	0.31637 (10)	0.01507 (10)	1.30 (7)	1
Bi2	0	0	0	3.1 (8)	0.142 (17)
Mg	0	0	0	3.1 (8)	0.858 (17)
O1	0.6844 (16)	0.6844 (16)	0.6844 (16)	3.2 (5)	1
O2	0.6237 (15)	0.7530 (18)	0.979 (3)	3.2 (5)	1
O3	0.900 (2)	0.900 (2)	0.900 (2)	3.2 (5)	1
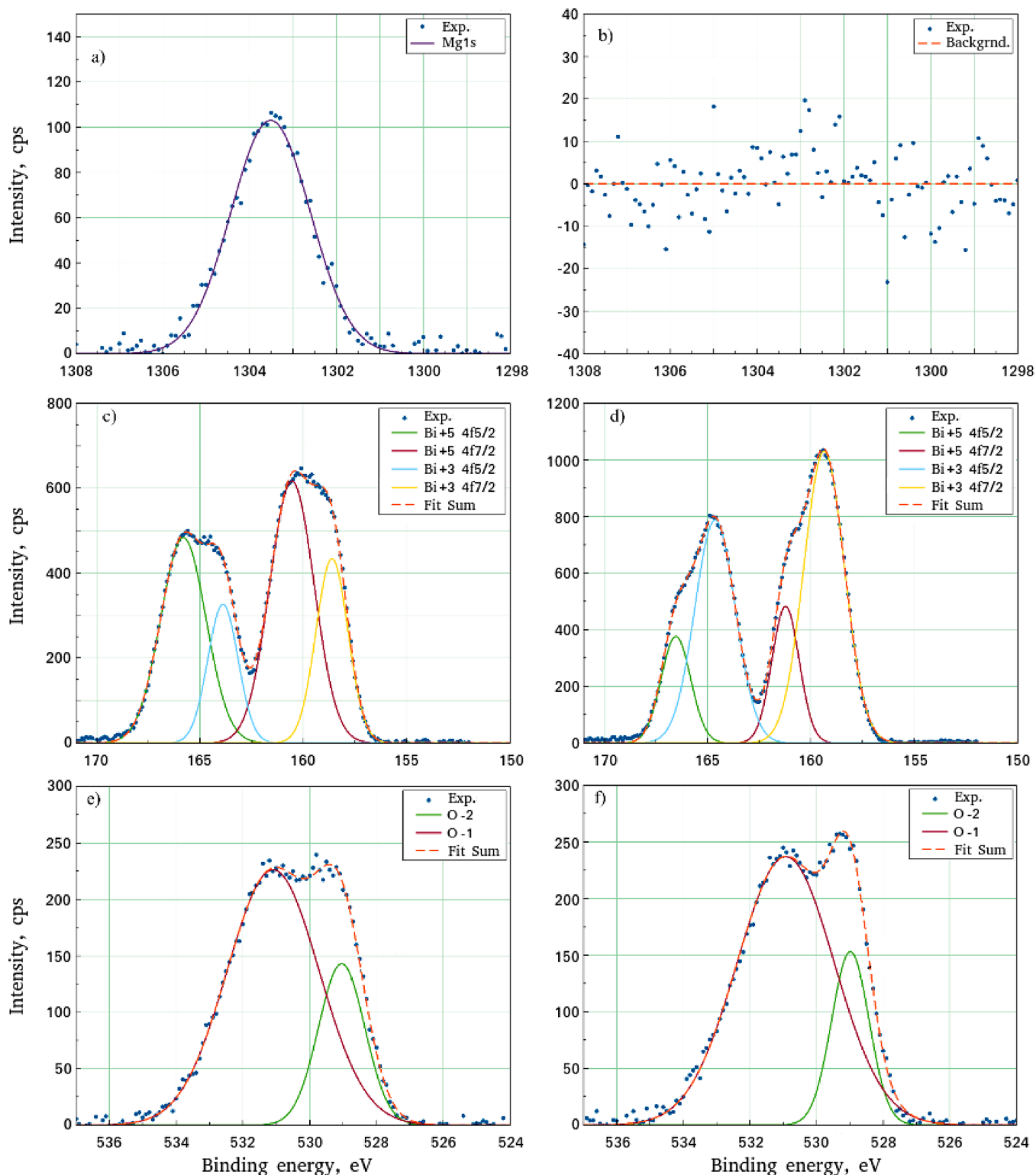
Figure 4. XPS spectra of MgBiO-7.69 (left) and MgBiO-1.00 (right): Mg 1s, top row; Bi 4f5/2 and Bi 4f7/2, middle row; and O 1s, bottom row.

0.97% and 6.02%, respectively, which are sufficiently close to the expected values of 1% for MgBiO-1.00 and 7.69% for MgBiO-7.69. These data serve as a solid indication of a different relative concentration of magnesium and bismuth in the cationic sublattices of the samples.

It has been shown above that the bismuthate samples should contain Bi^{5+} cations. In addition, XRD, EDX, and ICP-MS analyses demonstrate that a MgBiO-1.00 sample whose composition can be expressed as $Bi_{24.28(3)}Mg_{1.72(3)}O_{40}$ has a smaller amount of Mg than the MgBiO-7.69 sample described as $Bi_{24.05(3)}Mg_{1.95(3)}O_{40}$. Further insights into the chemical composition of the samples are given by the XPS spectra in Figure 4.

The spectral line Mg 1s of the MgBiO-7.69 sample in Figure 4a can be fitted well by a Gaussian curve with a maximum of 1303.5 eV. This binding energy is characteristic of Mg in
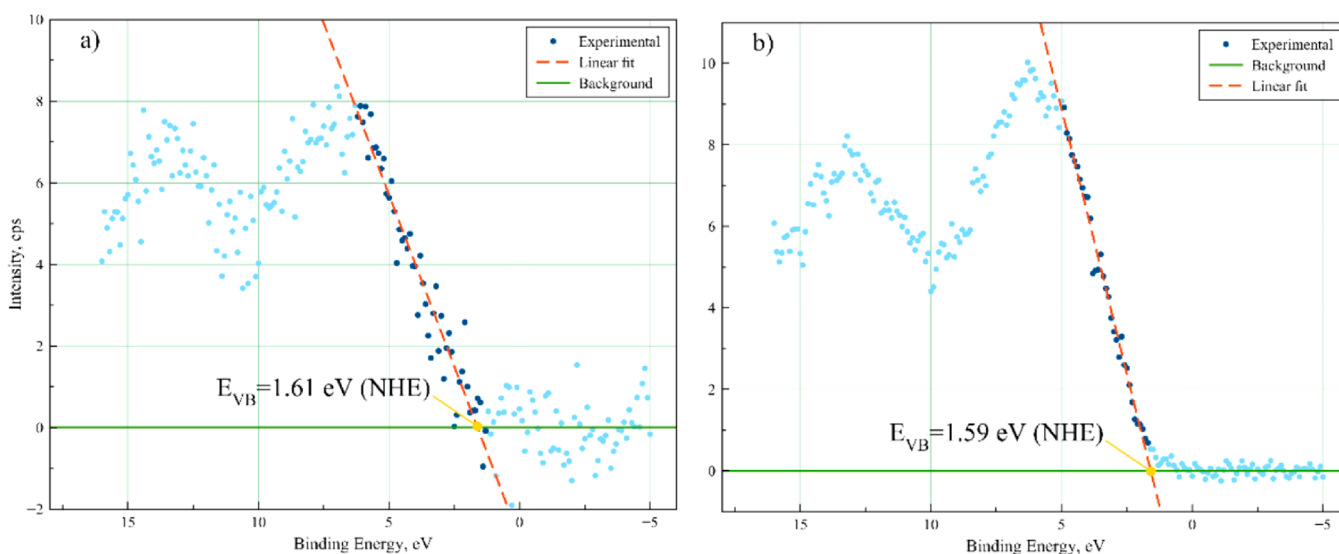
Figure 5. XPS spectra of (a) MgBiO-7.69 and (b) MgBiO-1.00 samples in the O 2p region. The horizontal line is the XPS baseline, whereas the vertical line is the linear extrapolation of the low-energy edge. The energies are given relative to NHE.[41]
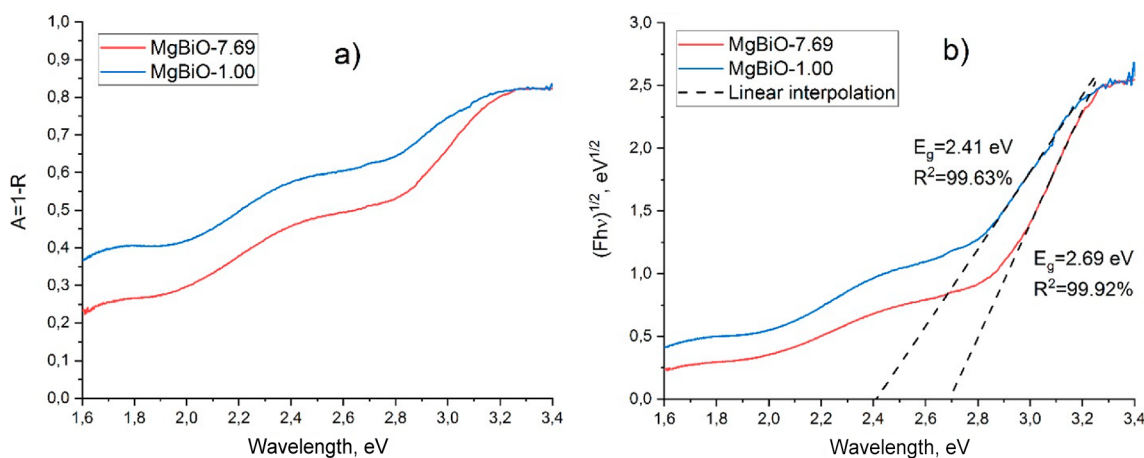

Figure 6. (a) Absorption spectra of bismuthates and (b) Tauc plots assuming the allowed indirect electronic transition model.

double oxides, e.g., $MgAl_2O_4$.[36] In contrast, the XPS spectrum of MgBiO-1.00 in the same energy range (Figure 4b) reveals no Mg at the particle's surface. Here, we remind the reader that XPS aims to study the surfaces of materials. Therefore, the absence of Mg at the MgBiO-1.00 particle's surface should be interpreted as the MgBiO-1.00 sample having a content of Mg that is lower than that of the MgBiO-7.69 sample.

In the samples, bismuth has two characteristic spectral lines located close to each other: Bi 4f5/2 and Bi 4f7/2. Each of them can be represented by a sum of two Gaussian curves. In the case of MgBiO-7.69 (Figure 4c), Gaussian curves representing the Bi 4f5/2 line have maxima at 163.89 and 165.8 eV. The Bi 4f7/2 spectral line of the same compound is represented by Gaussian curves with maxima at 158.61 and 160.55 eV. For each spectral line, the lower-binding energy Gaussian curves (with maxima at 163.89 eV for Bi 4f5/2 and 158.61 eV for Bi 4f7/2) are known to correspond to the Bi^{3+} cation in complex oxides.[37] The shift of the Gaussian curves toward higher energies is associated with the presence of the Bi^{5+} cation that was studied in detail previously.[38,39] The MgBiO-1.00 XPS spectra in Figure 4d also feature both Bi^{5+} (with binding energy maxima at 166.53 and 161.22 eV for 4f5/

2 and 4f7/2 electrons, respectively) and Bi^{3+} (with binding energy maxima at 164.63 and 159.36 eV for 4f5/2 and 4f7/2 electrons, respectively) lines. Here, the difference in the relative intensities of the Bi^{3+} and Bi^{5+} lines is important. That is, in MgBiO-7.69, the characteristic Bi^{5+} lines are more intense that the Bi^{3+} lines. The situation is the opposite in MgBiO-1.00, which is consistent with the fact that it contains fewer Mg^{2+} and Bi^{5+} cations.

The O 1s spectral line of MgBiO-7.69 in Figure 4e can also be approximated by two Gaussian curves. The maxima of the curves at 529 and 531.3 eV correspond to O^{2-}[40] and O^-, respectively. The presence of O^- in bismuthates of alkaline-earth metals, for instance, in several strontium bismuthates has been described previously.[12] Akin to MgBiO-7.69, the O 1s spectral line of the MgBiO-1.00 sample in Figure 4f is a superposition of two lines. One of them with a maximum at 529 eV corresponds to O^{2-}, while another with a maximum at 531 eV is due to O^-.

We note that no traces of carbon were detected in the XPS spectra described above. Such carbon traces have been found previously on a surface of strontium bismuthates.[12] This difference in the XPS spectra of strontium and magnesium
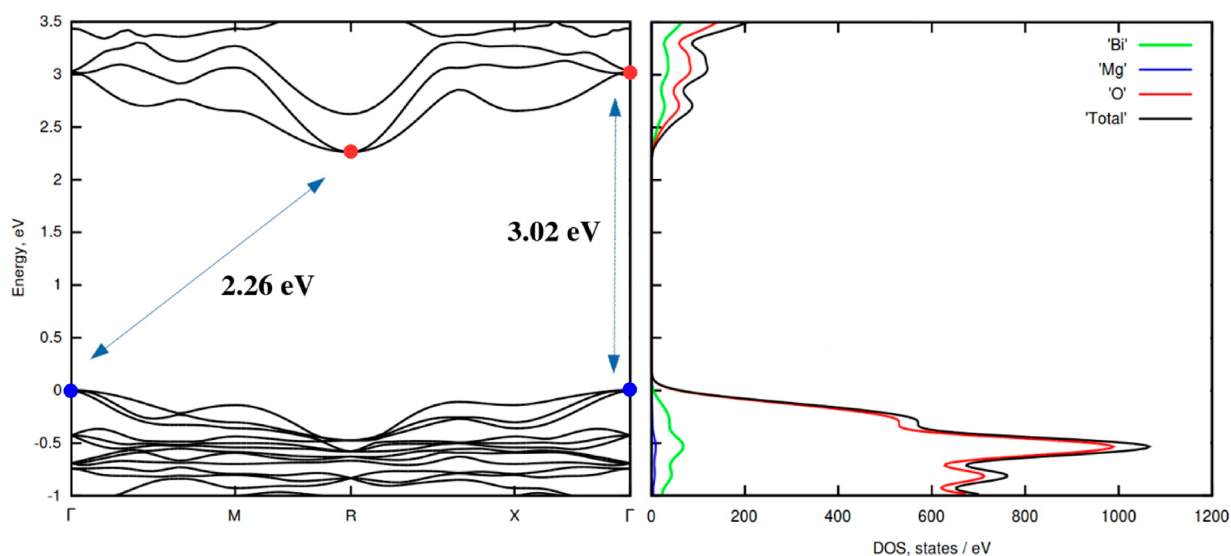
Figure 7. Computed band structure (left) and electronic density of states (right) of $Bi_{12}MgO_{20}$. The direct (3.02 eV) and indirect (2.26 eV) bandgaps are depicted.
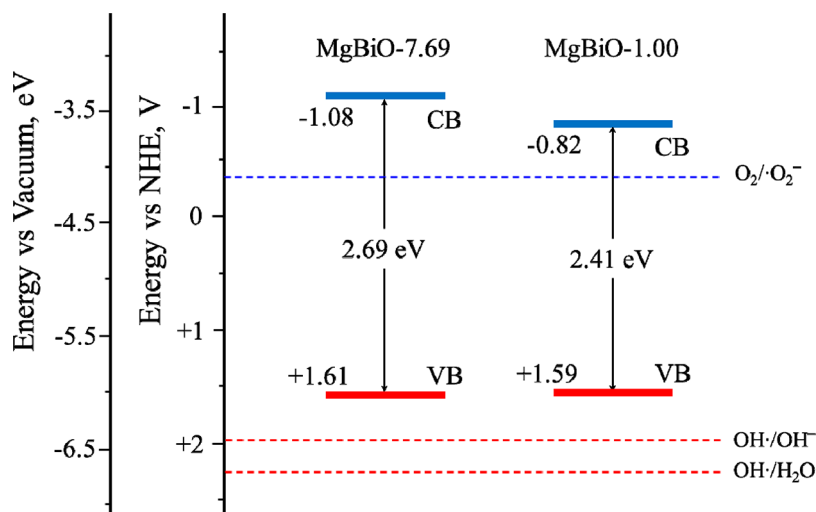

Figure 8. VB and CB positions of the magnesium bismuthates with respect to vacuum and electrochemical scales. The dashed lines denote the electrochemical potentials of some important oxidation and reduction half-reactions.

bismuthates comes from a higher affinity for carbon of the former compared to that of the latter.

4.2. Electronic Structure of the Magnesium Bismuthates. The electronic band structure of a semiconducting material schematically represents its valence and conduction bands (VB and CB, respectively) as well as its bandgap. In this work, we report the energies of the VBs and CBs of magnesium bismuthates relative to the normal hydrogen electrode's (NHE) potential. In our opinion, it is important that at least two of the three material's characteristics should be determined experimentally. On the basis of their values and the electrochemical potential of a chosen RedOx reaction, an energetic diagram can be drawn, which would demonstrate whether the synthesized bismuthates could act as a photocatalyst in such a reaction.

Here, the tops of VB potentials were determined as a low-energy edge of the O 2p line in the materials' XPS spectra (Figure 5). On this basis, we found values of 1.61 and 1.59 eV for MgBiO-7.69 and MgBiO-1.00, respectively. The difference

in VB potentials may be related to the lower contents of Mg^{2+} and Bi^{5+} in MgBiO-1.00 compared to those in MgBiO-7.69.

The bandgaps of the bismuthates were determined by diffuse reflectance spectroscopy. The recorded reflectance spectra are transformed into absorption ones using the equation $A = 1 - R$ (Figure 6a). According to the figure, both samples demonstrate significant extrinsic absorption (<3.2 eV). It is noteworthy that the MgBiO-1.00 sample containing less Mg is characterized by a higher absorbance over the entire visible range of light as compared to that of MgBiO-7.69. Importantly, absorption coefficients established near the intrinsic absorption edge enable the Kubelka−Munk transformation and application of the Tauc method to determine the bandgap. The Tauc plots obtained within the allowed indirect electronic transition model are depicted in Figure 6b. The bandgaps of the bismuthates can be obtained by extrapolating linear parts of the curves onto the x axis, which gives values of 2.69 and 2.41 eV for MgBiO-7.69 and MgBiO-1.00 samples, respectively.
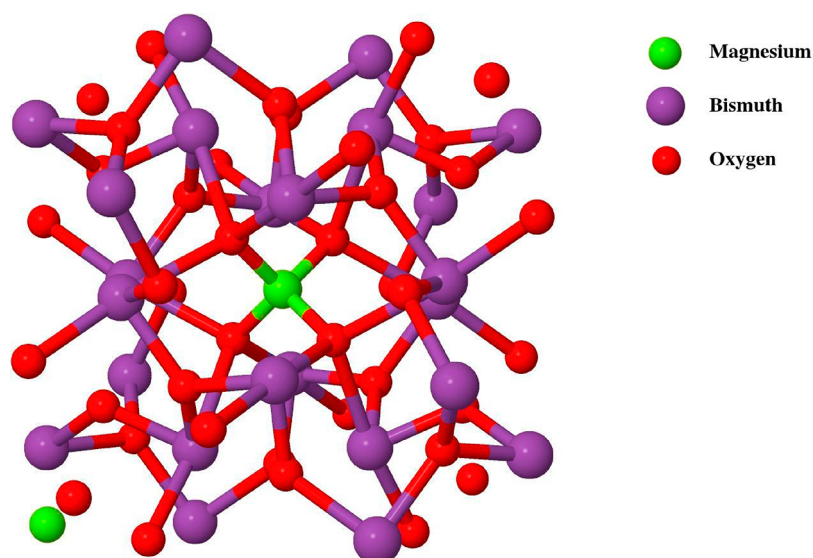
Figure 9. Ball-and-stick model of $Bi_{12}MgO_{20}$. For the sake of clarity, the doubled unit cell is depicted.
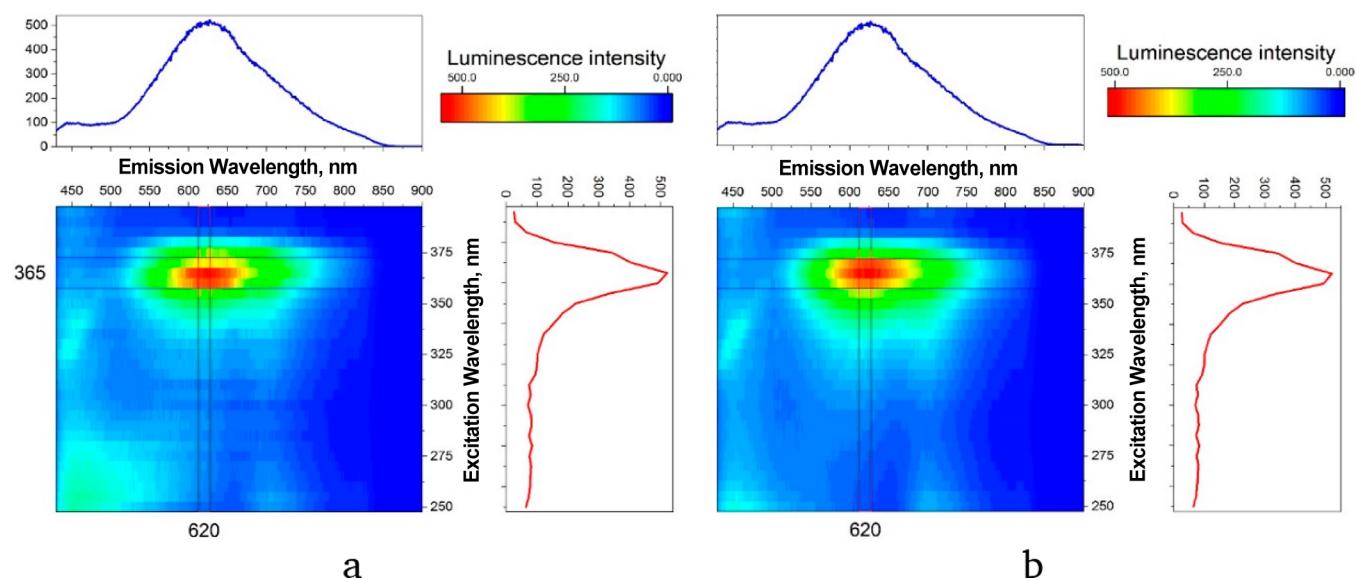

Figure 10. 2D luminescence maps of (a) the MgBiO-7.69 sample and (b) the MgBiO-1.00 sample: top, luminescence spectra at $\lambda = 365$ nm; bottom, luminescence excitation spectra registered at $\lambda = 620$ nm.

Thus, a decrease in the Mg^{2+} content of bismuthates leads to bandgap narrowing and an increase in extrinsic absorption.

In addition to the spectroscopic studies mentioned above, we aimed to model the electronic band structure of the bismuthates using periodic DFT calculations. Unfortunately, to match the small difference in Mg^{2+} concentration in the samples, such calculations would require prohibitively large supercells. For this reason, we consider the compound $Bi_{12}MgO_{20}$. Its band structure and electronic density of states are depicted in Figure 7. According to the figure, the magnesium bismuthate $Bi_{12}MgO_{20}$ is an indirect bandgap semiconductor with a bandgap of 2.26 eV. Given the fact that optical bandgaps are typically larger than the corresponding electronic ones, the bandgap of $Bi_{12}MgO_{20}$ (2.26 eV) is in a reasonable agreement with bandgaps of the MgBiO-7.69 (2.69 eV) and MgBiO-1.00 (2.41 eV) samples, determined from the Tauc plots (Figure 6b). The calculated electronic density of

the states indicates that both the VB and the CB of $Bi_{12}MgO_{20}$ are formed mainly from oxygen atomic orbitals.

On the basis of the determined VB tops in Figure 5 and the bandgaps in Figure 6b, we can draw the energetic diagrams of the bismuthates mentioned above (Figure 8). According to Figure 8, the VB's energy in the MgBiO-1.00 sample is lower than that in the MgBiO-7.69 sample by 0.02 eV. The CB's energy shift of 0.26 eV is an order of magnitude larger than that of the VB. Presumably, this band structure difference comes from the compositions of the different samples. In particular, it could be related to the different Bi^{5+} content demonstrated by XPS.

Figure 9 depicts a ball-and-stick model of $Bi_{12}MgO_{20}$ determined by XRD analysis. Therein, the magnesium atom is located at position (0.0; 0.0; 0.0). It is tetracoordinated, in other words, it is surrounded by four oxygen atoms. It is noteworthy that in accordance with the results of Rietveld refinement presented above, the model features $(Mg/Bi)O_4$
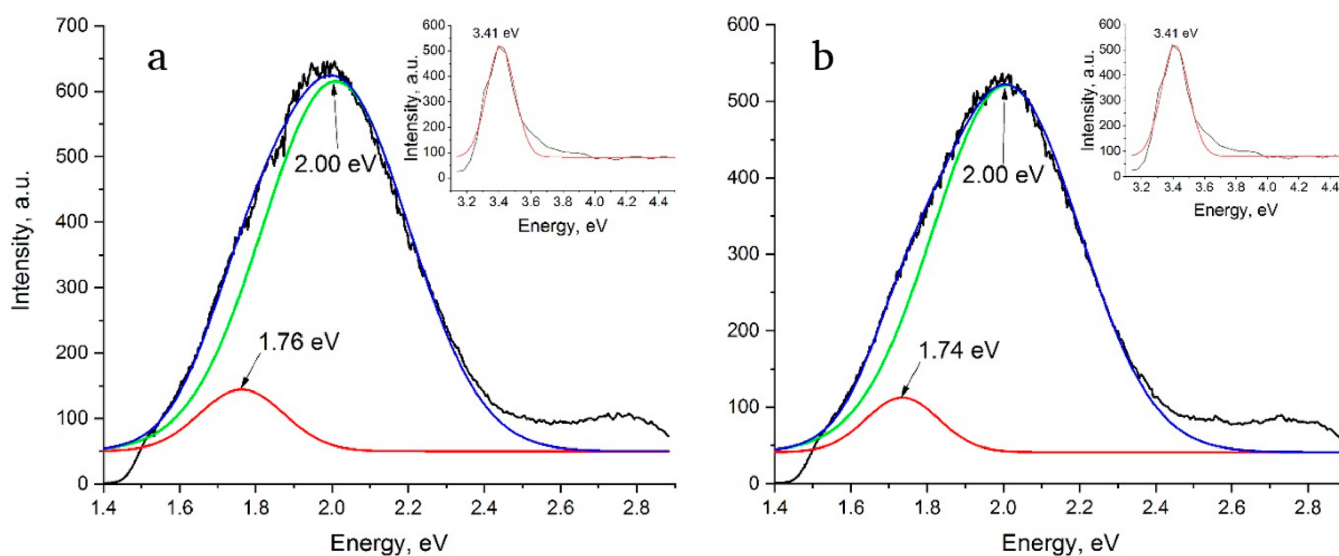
Figure 11. Luminescence spectra (unsmoothed black line) of (a) the MgBiO-7.69 sample and (b) the MgBiO-1.00 sample obtained at λ_{exc} = 365 nm. The red and green lines are Gaussians used for fitting, while the blue line is a cumulative fitting curve. Insets depict luminescence excitation spectra. The black line shows experimental data, and the red line is a Gaussian.
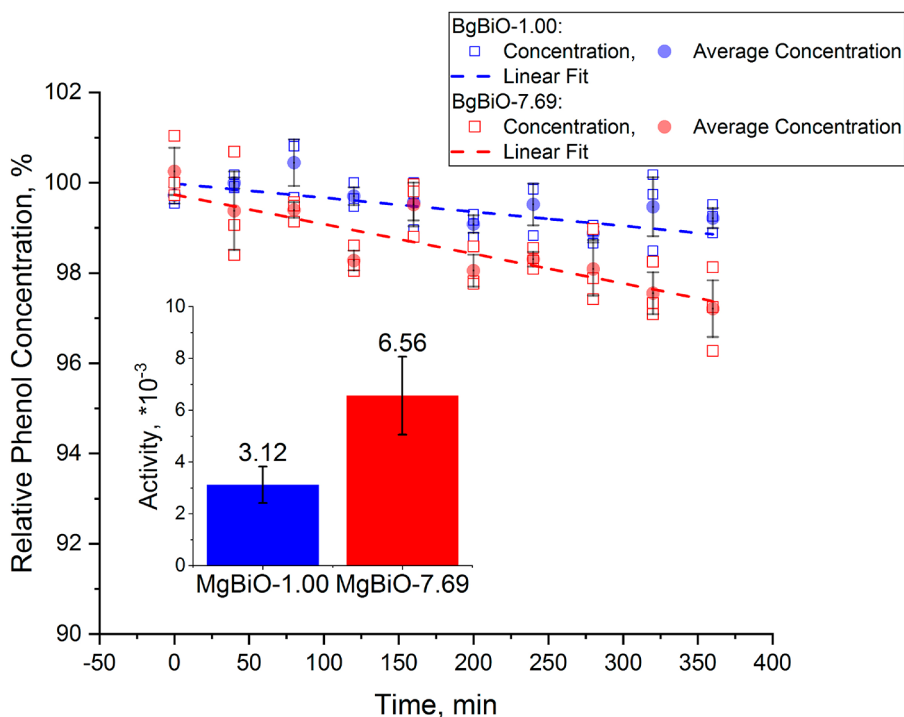

Figure 12. Relative concentration of phenol in its aqueous solution in the presence of the bismuthates as a function of irradiation time. The inset shows the rate of phenol degradation.

tetrahedra (see Figure 3). Thus, the computational model reflects both the structural peculiarities and the electronic properties of the prepared catalytic materials.

4.3. Luminescent Properties. The synthesized magnesium bismuthates demonstrate luminescent properties. Figure 10 shows that their two-dimensional (2D) luminescence maps are identical; the luminescence excited by a 365 nm light has a maximum at 620 nm. The luminescence spectra of the samples are presented in Figure 11. Therein, one can see that the spectral line of each sample can be fitted well by two Gaussian curves. The more intense Gaussian curve has the same position of the maximum (2.00 eV) in both bismuthates. The less

intense one has different positions of the maximum in samples MgBiO-7.69 (1.76 eV) and MgBiO-1.00 (1.74 eV). The luminescence excitation spectra of both samples are identical. The insets of Figure 11 show that the luminescence is most efficiently excited by a light, which is equivalent to 3.41 eV.

According to Figure 11, the luminescence is most efficiently excited by a light equivalent to ~3.4 eV. This energy is significantly higher than the optical bandgap (2.41−2.69 eV). Presumably, the latter corresponds to the computed indirect electronic bandgap of 2.26 eV. In addition to the indirect bandgap, calculations (see Figure 7) predict a direct bandgap of 3.02 eV. Taking this into account, we conclude that the

luminescence excitation takes place upon direct electron transfer from VB to CB.

On the basis of the studied luminescent properties, we can state that the bismuthates feature intrabandgap states, which may act as photocarrier traps thereby decreasing the photocatalytic activity of the materials.

4.4. Photocatalytic Activity. The photocatalytic activity of the bismuthates was tested in a simulated solar light-assisted phenol degradation reaction. The data presented in Figure 12 lead to the following two conclusions. First, the photocatalytic activity of the magnesium bismuthates in this reaction is very low. Second, it is strongly dependent on the sample being tested: the MgBiO-7.69 sample is >2 times more active than the MgBiO-1.00 sample.

To analyze the test results, let us refer to the energetic diagram in Figure 8. Because of the positions of VB tops in both bismuthates, no formation of $OH^{\bullet}$ radicals is possible from either hydroxyl groups or water presenting in the aqueous solution. In contrast, the position of the CB bottom is such that it enables the formation of superoxide radical $O_2^{-\bullet}$ from molecular oxygen, which is also present in the solution. Therefore, the photocatalytic activity of the bismuthates could be realized as promoting the following RedOx half-reactions: the formation of superoxide radical ion $O_2^{-\bullet}$ (reduction) and the direct photohole transfer (oxidation).

Admittedly, the proposed mechanism of the photocatalytic reactions is not unique. For instance, alternatively, organic molecules could form photodegradable surface complexes.[39] More detailed studies of the photocatalytic action of the magnesium bismuthates with a sillenite structure are forthcoming.

5. CONCLUSIONS

In this work, the synthesis of a novel photoactive compound with a general formula of $Bi_{26-x}Mg_xO_{40}$ is reported. It is demonstrated that by changing the Mg content one can affect the compound's band structure. Thereby, its bandgap as well as VB and CB potentials can be tuned. The luminescent properties of the material are revealed and investigated. In addition, the material's photocatalytic activity is found to be strongly dependent on its composition.

ASSOCIATED CONTENT

ⓈI Supporting Information

The Supporting Information is available free of charge at https://pubs.acs.org/doi/10.1021/acs.inorgchem.0c00486.

> SEM images, XRD patterns, EDX spectra, compositions of the samples, and mapping of the elements of the magnesium bismuthates (PDF)

Accession Codes

CCDC 1979140 and 1979141 contain the supplementary crystallographic data for this paper. These data can be obtained free of charge via www.ccdc.cam.ac.uk/data_request/cif, or by emailing data_request@ccdc.cam.ac.uk, or by contacting The Cambridge Crystallographic Data Centre, 12 Union Road, Cambridge CB2 1EZ, UK; fax: +44 1223 336033.

AUTHOR INFORMATION

Corresponding Author

> **Dmitry S. Shtarev** − *Yu. A. Kosygin Institute of Tectonics and Geophysics FEB RAS, 680000 Khabarovsk, Russia;* ⓞ orcid.org/0000-0002-1274-0183; Email: shtarev@mail.ru

Authors

> **Ruslan Kevorkyants** − *Saint-Petersburg State University, Laboratory "Photoactive Nanocomposite Materials", 199034 St Petersburg, Russia;* ⓞ orcid.org/0000-0002-2592-8353
>
> **Maxim S. Molokeev** − *Far Eastern State Transport University, 680000 Khabarovsk, Russia; Kirensky Institute of Physics, Federal Research Center KSC SB RAS, 660036 Krasnoyarsk, Russia; Siberian Federal University, 660041 Krasnoyarsk, Russia*
>
> **Anna V. Shtareva** − *Yu. A. Kosygin Institute of Tectonics and Geophysics FEB RAS, 680000 Khabarovsk, Russia*

Complete contact information is available at:
https://pubs.acs.org/10.1021/acs.inorgchem.0c00486

Notes

The authors declare no competing financial interest.

REFERENCES

(1) Valant, M.; Suvorov, D. A stoichiometric model for sillenites. *Chem. Mater.* **2002**, *14*, 3471−3476.

(2) Shtarev, D. S.; Shtareva, A. V.; Ryabchuk, V. K.; Rudakova, A. V.; Serpone, N. Considerations of Trends in Heterogeneous Photocatalysis. Correlations between conduction and valence band energies with bandgap energies of various photocatalysts. *ChemCatChem* **2019**, *11*, 3534−3541.

(3) Shtarev, D. S.; Ryabchuk, V. K.; Makarevich, K. S.; Shtareva, A. V.; Blokh, A. I.; Astapov, I. A.; Serpone, N. Calcium Bismuthate Nanoparticulates with Orthorhombic and Rhombohedral Crystalline Lattices: Effects of Composition and Structure on Photoactivity. *ChemistrySelect* **2017**, *2*, 9851−9863.

(4) Montalvo-Herrera, T.; Sanchez-Martinez, D.; Torres-Martinez, L. M. Sonochemical synthesis of $CaBi_6O_{10}$ nanoplates: photocatalytic degradation of organic pollutants (ciprofloxacin and methylene blue) and oxidizing species study (h+, ●OH, H_2O_2 and O_2^-●). *J. Chem. Technol. Biotechnol.* **2017**, *92*, 1496−1502.

(5) Liu, Z.; Wang, X.; Cai, Q.; Ma, C.; Tong, Z. $CaBi_6O_{10}$: A novel promising photoanode for photoelectrochemical water oxidation. *J. Mater. Chem. A* **2017**, *5*, 8545−8554.

(6) Shtarev, D.S.; Shtareva, A.V.; Syuy, A.V.; Pereginiak, M.V. Synthesis and photocatalytic properties of alkaline earth metals bismuthates − bismuth oxide compositions. *Optik* **2016**, *127*, 1414−1420.

(7) Shtarev, D. S.; Doronin, I. S.; Blokh, A. I.; Shtareva, A. V. Dependency of the optical properties of heterogeneous calcium bismuthate − bismuth oxide particles on the order of layers alternation. *Opt. Quantum Electron.* **2016**, *48*, 365.

(8) Shtarev, D. S.; Shtareva, A. V. Dependence of optical properties of calcium bismuthates on synthesis conditions. *J. Phys.: Conf. Ser.* **2016**, *735*, No. 012068.

(9) Wang, Y.; He, Y.; Li, T.; Cai, J.; Luo, M.; Zhao, L. Photocatalytic degradation of methylene blue on $CaBi_6O_{10}/Bi_2O_3$ composites under visible light. *Chem. Eng. J.* **2012**, *189−190*, 473−481.

(10) Wang, Y.; He, Y.; Li, T.; Cai, J.; Luo, M.; Zhao, L. Novel $CaBi_6O_{10}$ photocatalyst for methylene blue degradation under visible light irradiation. *Catal. Commun.* **2012**, *18*, 161−164.

(11) Tang, J. W.; Zou, Z. G.; Ye, J. H. Efficient photocatalytic decomposition of organic contaminants over $CaBi_2O_4$ under visible-light irradiation. *Angew. Chem., Int. Ed.* **2004**, *43*, 4463−4466.

(12) Shtarev, D. S.; Shtareva, A. V.; Ryabchuk, V. K.; Rudakova, A. V.; Murzin, P. D.; Molokeev, M. S.; Koroleva, A. V.; Blokh, A. I.; Serpone, N. Solid-State Synthesis, Characterization, UV-Induced Coloration and Photocatalytic Activity − The $Sr_6Bi_2O_{11}$, $Sr_3Bi_2O_6$, and $Sr_2Bi_2O_5$ Bismuthates. *Catal. Today* **2020**, *340*, 70−85.

(13) Shtarev, D. S.; Shtareva, A. V.; Molokeev, M. S.; Syuy, A. V.; Nashchochin, E. O. About Photocatalytic Properties of some Heterostructures Based on Strontium Bismuthate. *Key Eng. Mater.* **2019**, *806*, 161−166.

(14) Shtarev, D. S.; Shtareva, A. V.; Mikhailovski, V. J.; Nashchochin, E. O. On the influence of strontium carbonate on improving the photocatalytic activity of strontium bismuthate $Sr_6Bi_2O_{11}$. *Catal. Today* **2019**, *335*, 492−501.

(15) Obukuro, Y.; Matsushima, S.; Obata, K.; Suzuki, T.; Arai, M.; Asato, E.; Okuyama, Y.; Matsunaga, N.; Sakai, G. Effects of La doping on structural, optical, electronic properties of $Sr_2Bi_2O_5$ photocatalyst. *J. Alloys Compd.* **2016**, *658*, 139−146.

(16) Yang, Y.-C.; Wang, X.; Qu, J. Preparation and photocatalytic degradation of malachite green by photocatalyst $SrBi_4O_7$ under visible light irradiation. *Appl. Mech. Mater.* **2014**, *522−524*, 411−415.

(17) Zhou, W.; Yu, X. Use of $Sr_2Bi_2O_5$ as photocatalyst for the degradation of acid red G, Desalin. *Desalin. Water Treat.* **2011**, *30*, 295−299.

(18) Shan, Z.; Xia, Y.; Yang, Y.; Ding, H.; Huang, F. Preparation and photocatalytic activity of novel efficient photocatalyst $Sr_2Bi_2O_5$. *Mater. Lett.* **2009**, *63*, 75−77.

(19) Hu, X.; Hu, C.; Qu, J. Photocatalytic decomposition of acetaldehyde and Escherichia coli using $NiO/SrBi_2O_4$ under visible light irradiation. *Appl. Catal., B* **2006**, *69*, 17−23.

(20) Hu, C.; Hu, X.; Guo, J.; Qu, J. Efficient destruction of pathogenic bacteria with $NiO/SrBi_2O_4$ under visible light irradiation. *Environ. Sci. Technol.* **2006**, *40*, 5508−5513.

(21) Ge, J.; Yin, W.-J.; Yan, Y. Solution-Processed Nb-Substituted $BaBiO_3$ Double Perovskite Thin Films for Photoelectrochemical Water Reduction. *Chem. Mater.* **2018**, *30*, 1017−1031.

(22) Weng, B.; Xiao, Z.; Meng, W.; Grice, C. R.; Poudel, T.; Deng, X.; Yan, Y. Bandgap Engineering of Barium Bismuth Niobate Double Perovskite for Photoelectrochemical Water Oxidation. *Adv. Energy Mater.* **2017**, *7*, 1602260.

(23) Khraisheh, M.; Khazndar, A.; Al-Ghouti, M. A. Visible light-driven metal-oxide photocatalytic CO_2 conversion. *Int. J. Energy Res.* **2015**, *39*, 1142−1152.

(24) Yan, B.; Jansen, M.; Felser, C. A large-energy-gap oxide topological insulator based on the superconductor $BaBiO_3$. *Nat. Phys.* **2013**, *9*, 709−711.

(25) Tang, J.; Zou, Z.; Ye, J. Efficient Photocatalysis on $BaBiO_3$ Driven by Visible Light. *J. Phys. Chem. C* **2007**, *111*, 12779−12785.

(26) Ropp, R. C. *Encyclopedia of the alkaline earth compounds*; Elsevier, 2013.

(27) *Bruker AXS TOPAS V4: General profile and structure analysis software for powder diffraction data. User's Manual*; Bruker AXS: Karlsruhe, Germany, 2008.

(28) NIST X-ray Photoelectron Spectroscopy Database. https://srdata.nist.gov/xps/.

(29) Perdew, J. P.; Burke, K.; Ernzerhof, M. Generalized Gradient Approximation Made Simple. *Phys. Rev. Lett.* **1996**, *77*, 3865−3868.

(30) Perdew, J. P.; Burke, K.; Ernzerhof, M. Generalized Gradient Approximation Made Simple. *Phys. Rev. Lett.* **1997**, *78*, 1396−1396 (erratum).

(31) Gonze, X.; Amadon, B.; Anglade, P. M.; Beuken, J.-M.; Bottin, F.; Boulanger, P.; Bruneval, F.; Caliste, D.; Caracas, R.; Cote, M.; Deutsch, T.; Genovese, L.; Ghosez, Ph.; Giantomassi, M.; Goedecker, S.; Hamann, D.; Hermet, P.; Jollet, F.; Jomard, G.; Leroux, S.;

Mancini, M.; Mazevet, S.; Oliveira, M. J. T.; Onida, G.; Pouillon, Y.; Rangel, T.; Rignanese, G.-M.; Sangalli, D.; Shaltaf, R.; Torrent, M.; Verstraete, M. J.; Zérah, G.; Zwanziger, J. W. ABINIT: First-principles approach to material and nanosystem properties. *Comput. Phys. Commun.* **2009**, *180*, 2582−2615.

(32) Troullier, N.; Martins, J. L. Efficient pseudopotentials for plane-wave calculations. *Phys. Rev. B: Condens. Matter Mater. Phys.* **1991**, *43*, 1993−2006.

(33) Monkhorst, H. J.; Pack, J. D. Special points for Brillouin-zone integrations. *Phys. Rev. B* **1976**, *13*, 5188−5192.

(34) Williams, T.; Kelley, C.; Merritt, E. A.; Bersch, C.; Bröker, H.-B.; Campbell, J.; Cunningham, R.; Denholm, D.; Elber, G.; Fearick, R.; Grammes, C.; Hart, L.; Hecking, L.; Juhász, P.; Koenig, T.; Kotz, D.; Kubaitis, E.; Lang, R.; Lecomte, T.; Lehmann, A.; Lodewyck, J.; Mai, A.; Märkisch, B.; Mikulík, P.; Sebald, D.; Steger, C.; Takeno, S.; Tkacik, T.; van der Woude, J.; van Zandt, J. R.; Woo, A.; Zellner, J. *Gnuplot 5.2: An interactive plotting program*; 2018.

(35) Sillen, L. G. *X-Ray Studies on Bismuth Trioxide*; Arkiv för kemin, mineralogi och geologi Series; 1938; Vol. *12A*, pp 1−15.

(36) Haycock, D. E.; Nicholls, C. J.; Urch, D. S.; Webber, M. J.; Wiech, G. The electronic structure of magnesium dialuminium tetraoxide (spinel) using X-ray emission and X-ray photoelectron spectroscopies. *J. Chem. Soc., Dalton Trans.* **1978**, *12*, 1785−1790.

(37) Srivastava, P.; Saini, N. L.; Sekhar, B. R.; Garg, K. B. Core-level photoemission study on a Bi-2212 single crystal. *Mater. Sci. Eng., B* **1994**, *22*, 217−221.

(38) Hughes, M. A.; Fedorenko, Y.; Gholipour, B.; Yao, J.; Lee, T.-H.; Gwilliam, R. M.; Homewood, K. P.; Hinder, S.; Hewak, D. W.; Elliott, S. R.; Curry, R. J. n-type chalcogenides by ion implantation. *Nat. Commun.* **2014**, *5*, 5346.

(39) Sajjad, S.; Leghari, S. A. K.; Zhang, J. Nonstoichiometric Bi_2O_3: efficient visible light photocatalyst. *RSC Adv.* **2013**, *3*, 1363−1367.

(40) Kostikova, G. P.; Korol'kov, D. V.; Kostikov, Yu.P. Valence States of Lead and Bismuth Atoms in the High-Temperature Superconductor $BaPb_{1-x}Bi_xO_3$. *Russ. J. Gen. Chem.* **2001**, *71*, 1010−1012.

(41) Chambers, S. A.; Droubay, T.; Kaspar, T. C.; Gutowski, M.; van Schilfgaarde, M. Accurate valence band maximum determination for $SrTiO_3$ (001). *Surf. Sci.* **2004**, *554*, 81−89.